Universiteit Utrecht

Faculteit Bètawetenschappen

Improving the Description of Lateral Shower Profiles in the FoCal Detector Prototype

Bachelor Thesis

Valentijn Verbeek

Natuur- en Sterrenkunde

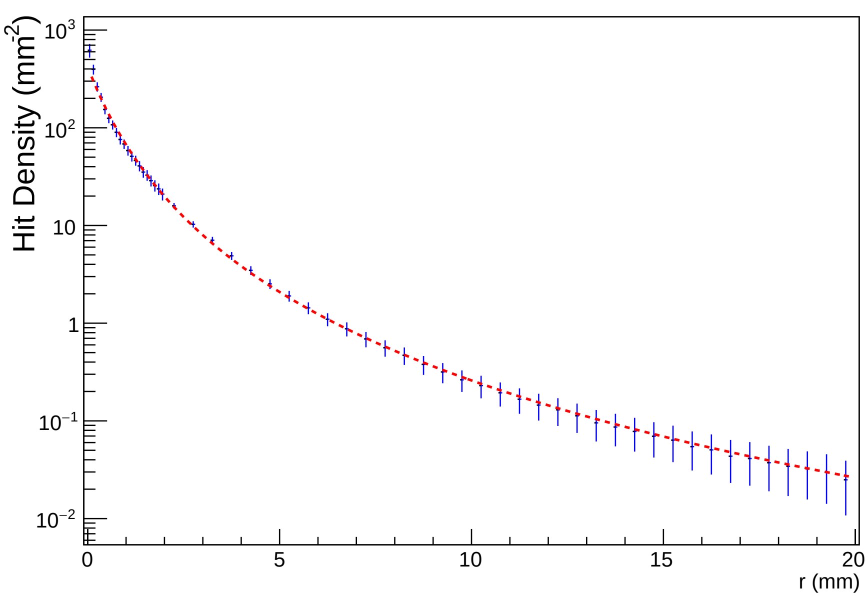

Supervisors:

Prof. Dr. T. Peitzmann
Institute for Subatomic Physics
Utrecht University

Dr. Ir. G.J.L. Nooren
Institute for Subatomic Physics
Utrecht University

13 juni 2018

Abstract

To get a better understanding of the fundamental laws and particles of the universe, a forward electromagnetic calorimeter (FoCal) is proposed for ALICE at CERN. A prototype detector has been build and is currently being analysed. This thesis focusses on finding an analytical description of the lateral hit density profiles of the prototype, obtained by measurements of the 50 GeV SPS beam at CERN. Unfortunatly, uncertainties of the hit densities from earlier analysis were lost and new uncertainties have been calculated, assuming pure Poisson fluctuations of the number of hits with a constant mean value per event. The new uncertainties are overestimated with the current approach, leading to difficulty in interpreting the fit results. From earlier analysis a power law function was deemed best fit for the profiles and in this thesis four adjustments are applied for new fits. The results are compared by looking at χ^2 values of the fits. All adjusted functions seem to perform better than the original and $g_1(r)$ performs best. Comparison between the results of the overestimated uncertainties and results obtained with underestimated uncertainties, shows similar behaviour of the fits. This could imply the functions are good to describe the data.

Contents

1 Introduction

To get a better understanding of the laws of nature, the structure of matter can be studied. So far it is shown by scattering experiments that hadrons, like protons and neutrons, are not fundamental particles and have constituents called *partons*. At the Large Hadron Collider (LHC) in CERN, such experiments are done to research properties of the Quark-Gluon Plasma (QGP). The QGP is a state of matter in which quarks and gluons are not in bound states, so they do not form protons and neutrons, allowing for research of the partons. One of the experiments researching the QGP is ALICE (A Large Ion Collider Experiment), in which heavy ions collide at high energies ($\sim$ TeV) to form the QGP. ALICE contains several detectors to obtain information of the particles and interactions in the QGP. To get more information about the structure of protons and the cores of the colliding particles, a forward electromagnetic calorimeter (FoCal) is proposed.

From *Deep Inelastic Scattering* experiments, we know protons consist of three quarks, called the valence quarks. These quarks are bound by the strong force, which is carried by gluons. A way to describe the structure of protons is by using *parton distribution functions* (PDFs). For these functions a variable called the Bjorken-x is used, which is described as the momentum of a parton as a fraction of the momentum of the proton during a collision. In scattering experiments, single partons are the colliding particles and knowing their energy before colliding will give more information about the structure of protons. For higher energies, more gluons will be created with a low x value. In this low x regime, the PDFs are not well determined and theoretical calculations predict non-linear behaviour, causing gluon saturation. An approximate description of this x value is given by:

$$x \approx \frac{2p_T}{\sqrt{s}} e^{-y} \tag{1}$$

in which $\sqrt{s}$ is the center of mass energy and y and p_T are the rapidity and transverse momentum of the outgoing parton respectively. Rapidity is a measure of relativistic velocity and for high energies it can be approximated by pseudorapidity η, which describes the angle of a particle relative to the beam axis:

$$\eta = -\log(\tan(\frac{\theta}{2})) \tag{2}$$

Here θ is the angle between the momentum of the particle and the beam axis. From these equations you can see that for high energy and high rapidity, particles will have a small angle with the beam axis.

The predicted gluon saturation could be explained by the *Colour Glass Condensate* (CGC) model. Parton interactions in the CGC will cause direct photons to be emitted. Photons with high rapidity will have small angles with the beam axis and the FoCal will measure these direct photons, which will give information about the gluon density of the colliding particles. This means the FoCal project is interested in the low x regime. The FoCal detector can detect direct photons if it is placed close to the beam pipe, at a large distance from the interaction point. Other particles, such as π^0, will also be produced by the collision. These pions can decay into two photons, which will be detected too by FoCal. The detector should be able to seperate these photons from the direct photons because of the high granularity layers. More details of the FoCal prototype will be discussed in section 3. For more in depth details refer to [1].

To know how a photon shower looks in the detector, lateral hit density profiles of showers will be studied. The theory relevant to these showers will be discussed in section 2. The goal of this thesis is to study these profiles by looking at possible analytical descriptions of the data. This will be discussed in section 4. The relevant analysis of the available data, like determining shower position and several fit possibilities, will also be discussed. Due to technical difficulties, parts of data analysis were lost during the research period. To continue with the available data, new calculations for the uncertainties in hit densities were used. In section 4.2 the applied method for calculating new uncertainties will be discussed. General uncertainty calculations can be found in appendix A.

2 Theory

During a photon shower, more particles are produced. Each type of produced particle has different interactions with matter. The particles of interest for FoCal are electrons, positrons and photons. The different ways to detect these particles, the interactions with matter and properties of electromagnetic showers will be discussed in the following subsections.

2.1 Electrons and positrons

Charged particles can lose energy via several processes. At high energies, the energy loss is dominated by *bremsstrahlung*. In this process the particle loses energy by emitting a photon when moving through an electrical field of another charged particle. For lower energies, processes like *ionization* start to play a role. In figure 1 you can see which processes dominate at which energies. The particles for FoCal are in the range of several GeV, so bremsstrahlung seems to be the most important process. The energy loss for electrons due to bremsstrahlung is:[2]

$$\frac{dE}{dx} = 4\alpha N_A \frac{Z^2}{A} r_e^2 \cdot E \ln\left(\frac{183}{Z^{\frac{1}{3}}}\right) \tag{3}$$

In this equation α is the fine-structure constant, N_A the constant of Avogadro, Z the atomic number, A the mass number and r_e the electron radius. This shows that a material with high atomic number will cause more energy loss for the electron passing through it.

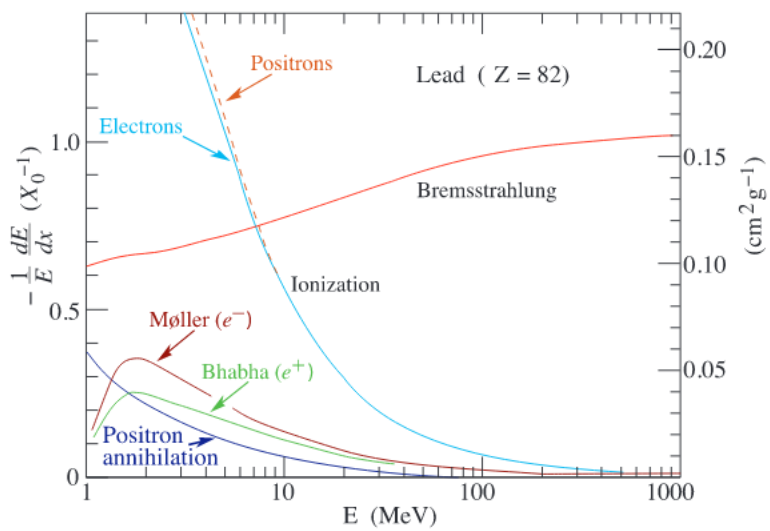

Figure 1: Fractional energy loss per radiation length in lead as a function of energy of electrons. For high energies bremsstrahlung is dominant, for lower energies ionization will play a role and for even lower energies Møller and Bhabha scattering will lead to δ-ray production. Taken from [3].

2.2 Photons and photon showers

Unlike electrons and positrons, a photon has no mass or charge. Therefore it interacts differently with matter. For high energies, when a photon interacts with a nucleus, it will convert into an electron-positron pair. This is called *pair production*. The electron and positron will then interact as described in the previous section, causing a cascade of interactions, also called an *electromagnetic shower*. In the shower, particles will lose energy by bremsstrahlung and pair production, increasing the number of particles, untill the *shower maximum*, where the energy has dropped such that most particles no longer have enough energy to continue the cascade. An example of an electromagnetic shower is shown in figure 2.

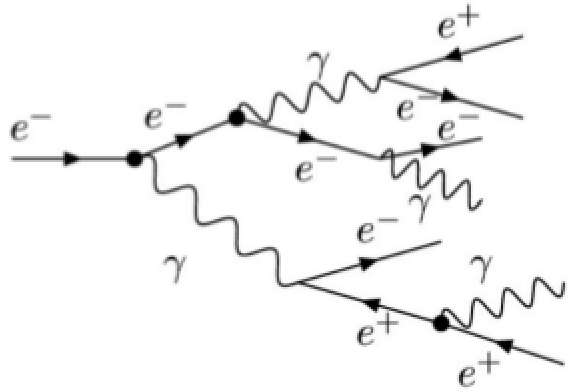

Figure 2: Example of electromagnetic shower with bremsstrahlung and pair production. Taken from [4].

2.2.1 Electromagnetic shower properties

When particles move through matter, a measure for the length at which interactions occur can be defined. This characteristic length is called the radiation length X_0. It is defined as the distance over which an electron loses all but $1/e$ of its energy by bremsstrahlung. For a pair-producing photon it is $\frac{7}{9}$ of the mean free path (see [3]). A way to approximate X_0 is:[5]

$$X_0 = \frac{180A}{Z^2}\frac{\mathrm{g}}{\mathrm{cm}^2} \tag{4}$$

By measuring the radiation length in g/cm^2 one can easily compare it with materials of different density ρ. When more than one material is used, X_0 can be calculated with:

$$\frac{1}{X_0} = \sum_i \frac{V_i}{X_{0,i}} \tag{5}$$

where V_i and $X_{0,i}$ are the fraction of volume and the radiation length of a single type of material respectively.

In an electromagnetic shower there is a critial energy E_c, defined as the point when the bremsstrahlung rate equals the ionization rate. For electrons in solids this critical energy is:[5]

$$E_c = \frac{710\ \mathrm{MeV}}{Z + 1.24} \tag{6}$$

While developing, the shower will widen because of two processes. Scattering and production of particles will move them away from the shower axis.[6] An important property to describe electromagnetic showers is the Molière radius R_M, which is the mean lateral displacement from multiple coulomb scattering for electrons at the critical energy when passing through $1X_0$ of material. In a cylinder with radius equal to one R_M centered around the shower center, 90% of the shower energy is contained. Roughly 99% of the energy will be absorbed in $3.5R_M$. The way to calculate R_M is given by:[5]

$$R_M = \frac{21.2\mathrm{MeV}}{E_c}X_0 \tag{7}$$

2.3 Calorimeters

The FoCal prototype is a calorimeter. Calorimeters measure energy of particles by absorbing them. Two different types of calorimeters exist: electromagnetic and hadronic calorimeters. Electromagnetic calorimeters are mainly used to measure electrons and photons through their electromagnetic interactions, like bremsstrahlung and pair production. Hadronic calorimeters are mainly used to measure hadrons through their strong and electromagnetic interactions. Further distinctions can be made by the construction of the calorimeter. If the detector is made of alternating layers consisting of absorber material and active material, it is called a sampling calorimeter. Another way to construct calorimeters is by using one material for both the absorbing and active layers, which is called a homogeneous calorimeter. More distinctions can be made between digital and analog calorimeters, which has to do with the readout. For high granularity, digital readout is preferred.

In general, calorimeters have certain features. They measure both charged and neutral particles. They have different responses to electrons, muons and hadrons, so these particles can be seperated in measurements. The position of incoming particles can be measured. For increasing energy of incoming particles, the size of the calorimeter should grow logarithmically.

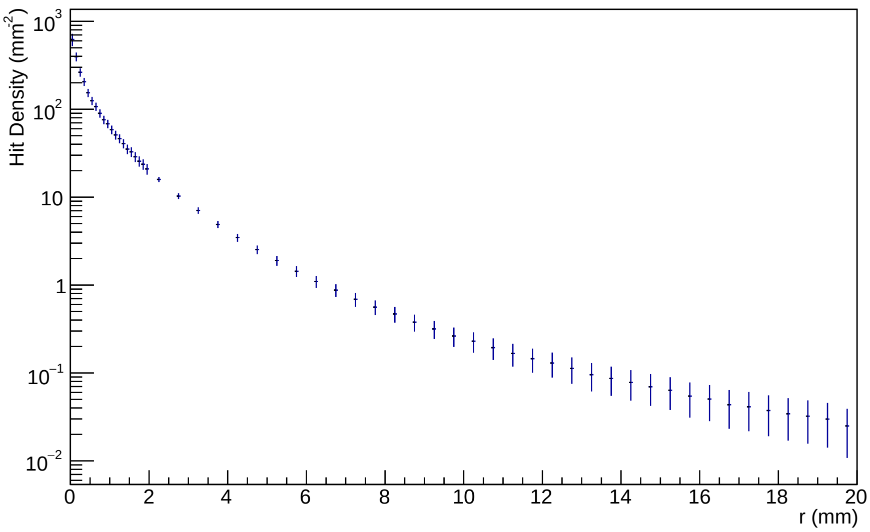

Figure 3: Example of a lateral hit density profile.

2.3.1 Lateral Profiles

The lateral hit density profiles used for this thesis show the hit density as a function of radius r from the shower center. To obtain these profiles, the signal of the measured particles is used to calculate the number of hits and then the hit densities, which will be discussed in section 4. An example of a lateral profile can been seen in figure 3. Since the profile is represented logarithmically in the y-axis, one can conclude that a single exponential function can not describe the profile. Earlier research suggests several functions to describe these profiles:

- A sum of two exponentials:[6]

$$f_1(r) = A_1[p \cdot e^{-r/\lambda_1} + (1-p) \cdot e^{-r/\lambda_2}] \tag{8}$$

- The sum of an exponential and an exponential of the square root of the distance r to shower axis:[7]

$$f_2(r) = A_1[p \cdot e^{\sqrt{-r/\lambda_1}} + (1-p) \cdot e^{-r/\lambda_2}] \tag{9}$$

- A sum of two lorentzians:[8]

$$f_3(r) = A_1[p \cdot \frac{2R_1^2}{(r^2+R_1^2)^2} + (1-p) \cdot \frac{2R_2^2}{(r^2+R_2^2)^2}] \tag{10}$$

- A modified power law:[9]

$$g_0(r) = p_0(1 + \frac{r}{p_1 \cdot p_2})^{-p_1} \tag{11}$$

3 FoCal

As discussed in section 1, the FoCal is a proposed forward electromagnetic calorimeter for ALICE. It will be placed at a distance of 7 m from the interaction point. Figure 4 gives a schematic view of the placement. The prototype is a Si/W sampling calorimeter consisting of 24 layers and uses CMOS sensors of MIMOSA−A type of *Monolithic Active Pixel Sensors* (MAPS). Tungsten was chosen as the absorber, because it will lead to small R_M. For the samplers, high-granularity silicon sensors were chosen to get high detail of the spatial distribution of showers. In the following subsections, more detailed properties of the prototype and the measurements that were done so far will be discussed.

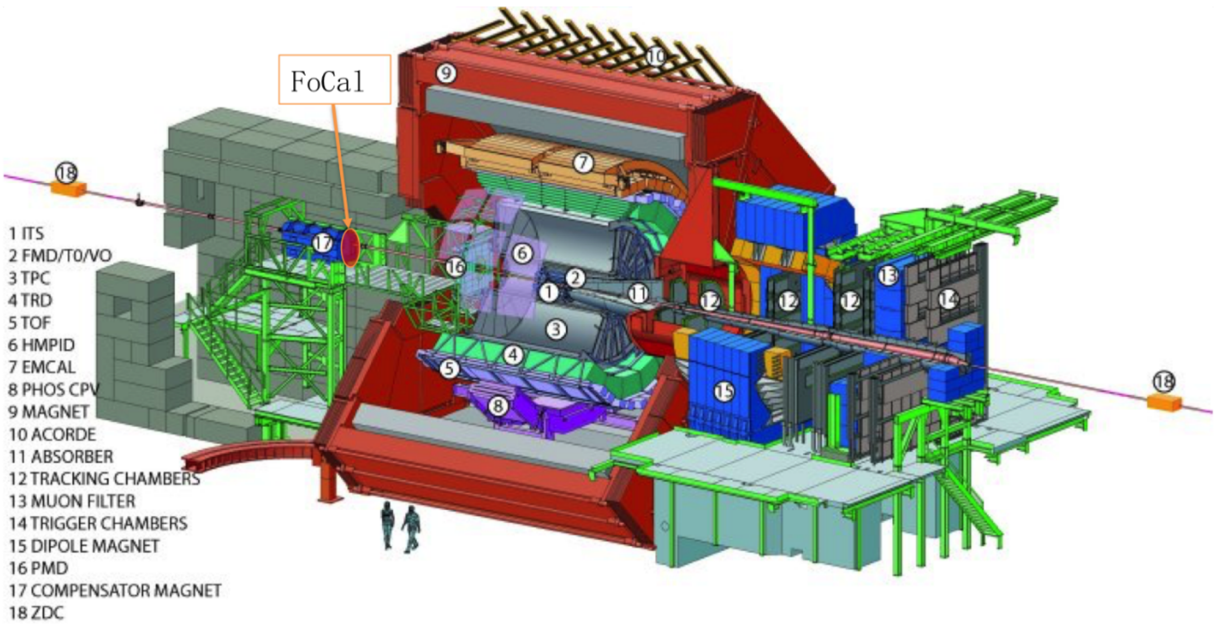

Figure 4: Schematic view of the proposed placement of FoCal in ALICE. Taken from [10].

3.1 Layers

Each layer of the prototype has a thickness of 4 mm, filled with 3 mm tungsten and 1 mm of material related to the sensors. This corresponds to $0.97X_0$ per layer. For the first active layer, called layer 0, the front half of the absorber was replaced by aluminium, leading to a thickness of $0.03X_0$, in order to measure particles before the start of the shower. At $20X_0$ a tungsten block of 2 cm is placed, so the total thickness is 116 mm, which is equivalent to $28X_0$. This is done to make sure most of the showers are contained within the detector. The coordinate system used for data analysis has the center of the first layer as its origin. The z axis is along the beam direction, the longitudinal direction of the detector. The x and y axis are parallel to the plane of the layers, with x horizontally.

Looking in the transverse direction, the size of the active area per layer is 4×4 cm^2, while the absorber measures 5×5 cm^2. Each layer has two modules, each with two senors, with alternating orientation, so the sensors cover opposite halves of the detector. See figure 5 for more detail. The design creates a narrow gap between the sensors in the x direction and an overlap in the y direction, which is accounted for in earlier data analysis in [5]. The overlap minimises the insensitive areas of the detector. Up to 500 GeV, 95% of the shower energy will be contained in the prototype and the calculated Molière radius is $R_M = 10.5$ mm (see [10]), which makes it possible for the prototype to be relatively small.

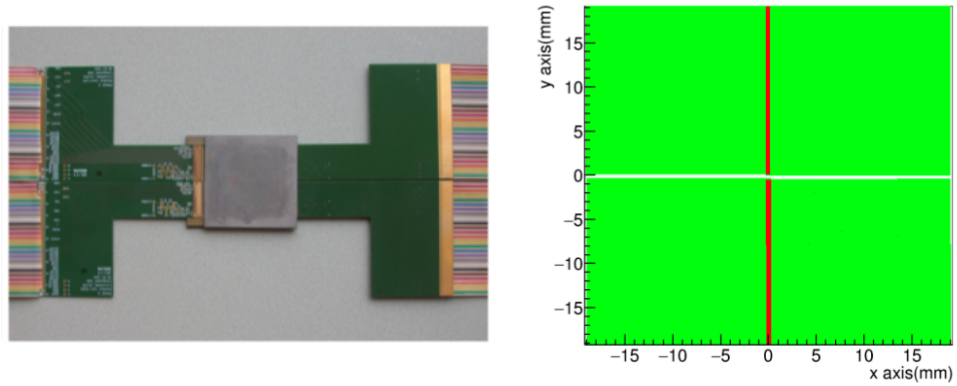

Figure 5: Left: photo of a layer. Right: schematic example of the gap (white space) and overlap (red space) of sensors (green space). Taken from [5].

3.2 Sensors

Each sensor has a total size of 19.52×20.93 mm^2 with 640×640 pixels in an active area of 19.2×19.2 mm^2. Each pixel has a size of 30×30 μm^2, leading to a binary readout with a total of ~ 39 million pixels for the whole prototype. Because of the large amount of pixels, dedicated printed circuit boards (PCB) were made, onto which the sensors are connected.

Incoming particles are detected by the pixels, which collect the charge deposited by the particle and convert it into a digital binary signal. Pixels are grouped into four channels with a size of 160×640 pixels and every channel is driven at 160 MHz. Every line of pixels has a readout time of 1 μs and is handled by a discriminator. All lines of pixels are read out sequentially and the sensors are read out in parallel, leading to a total readout time of 640 μs.

The chosen sensor dissipates more heat than conventional sensors. However, the heat conductivity of tungsten is high enough to transport heat to the outside of the chip, which means the cooling elements can be connected at the edges. This helps with the compactness of the prototype, since there is no need for seperate cooling layers. For cooling, water at a temperature of 17^oC is used to keep the sensor at a temperature of $\sim 27^o$C. When the temperature of the absorber rises above 35^oC, the power supply will be shut down. See figure 6 for a visual representation of the cooling system.

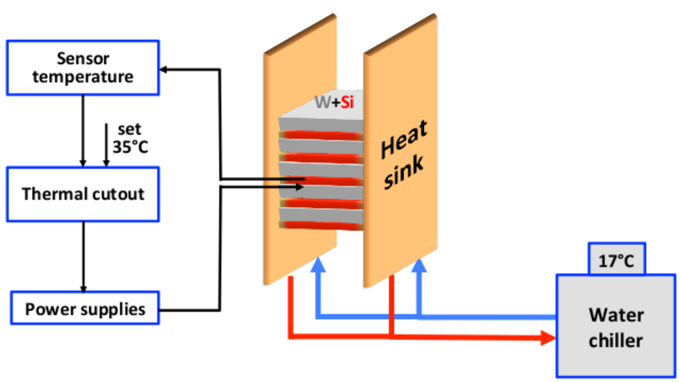

Figure 6: Schematic view of the cooling and temperature protection system. Taken from [10].

3.3 Scintillators

The detector can not take data constantly during beam measurements, so it needs a trigger to determine when a particle passes through it. For these triggers five scintillators are used, called Presence (P), Front (F), Horizontal (H), Vertical (V) and Back (B). The positioning of the scintillators can be seen in figure 7. Using multiple scintillators makes sure that fake triggers due to noise can be filtered. Combinations of the scintillators used for triggers are PF, HVF and BF. HF is used as a check for HVF. When measuring cosmic rays, the detector has two NE102a scintillators and uses the BF combination.

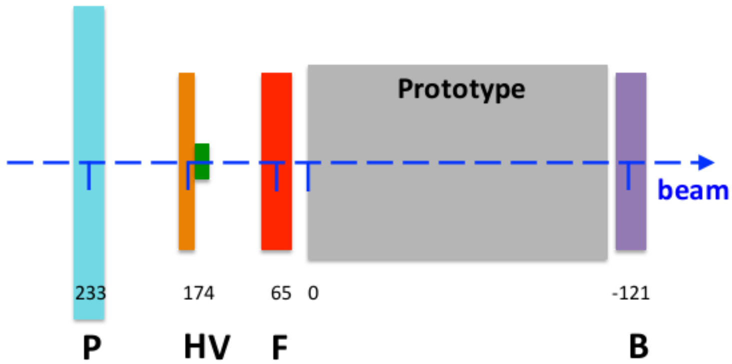

Figure 7: Setup of trigger scintillators for measurements. The numbers indicate distance on beam axis in mm. Taken from [10].

3.4 Data acquisition system

The PCB of the sensor is connected to the readout board via a flat cable. During measurements, roughly 8 GB/s of data is generated. The writing speed of the computer is not high enough to process all data at once. To manage this, several *field programmable gate arrays* (FPGAs) are used in combination with a local buffer memory. A full readout of a sensor is called a *frame*. The buffer can collect 814 frames before it is full. This collection of frames is called a *spill* and the collection of multiple spills is called a *run*. All data is send to the *data acquisition* (DAQ) computer via ethernet, which takes about 2 minutes. To keep the data stream in phase between all chips, clock synchronisation is done between sensors. For each layer one sensor is chosen for the clock synchronisation.

The FPGAs run an embedded Linux system and the DAQ software is developed using ROOT based on C++. The data transfer protocol uses TCP/IP. There are three options for the read-out method: beam mode, pedestal mode and cosmic mode. The beam mode is an external-trigger mode, in which all frames are collected and the data is send to the DAQ computer. During data transfer, data taking is suspended. Pedestal mode is a self-trigger mode, in which data is continuously transfered to the buffer and send to the DAQ server when the buffer is full. Data taking is also suspended during transfer. Cosmic mode is an external-trigger mode used for measurements of cosmic rays. In this mode three adjacent frames are immediatly transferred to the DAQ server.

3.5 Measurements

The prototype was used for measurents at DESY (Deutsches Elektronen-Synchrotron), CERN SPS (Super Proton Synchrotron) and Utrecht. The data used for analysis in this thesis are from the SPS measurements, so these will be discussed.

For the measurements at SPS a mixed beam, containing electrons and pions, was provided with energies of 30, 50, 100 and 244 GeV. For each energy, the relative amount of electrons and pions was different. Since the Cherenkov system could not provide appropriate signals at high momentum, there was no external detector for particle identification. The identification process was done during data analysis in [5]. From this earlier data analysis lateral profiles for each layer were made, which will be discussed in the next section.

4 Data Analysis

For the analysis in this thesis, data was used from the SPS measurements with energies of 50 GeV. Earlier analysis (see [5] and [10]) included event selection, tracking, alignment, determining shower position, measuring inclination of the beam, calculating hit densities and calibration of the detector. A summary of this analysis will be discussed below, followed by analysis of the lateral profiles.

4.1 Earlier Analysis

As discussed in section 3.5, the beam used at SPS is not a pure electron beam, so the beam particles need to be identified. One event can contain a single electromagnetic or hadronic shower, a track, noise or a mixture of these. Events are selected by cutting off events with pileup based on trigger information, which excludes most events with more than one particle. Then a selection is applied on the total number of hits N_{hits}: events with small number of hits and events with too many hits are excluded. For the events with two particles that are still left, a cut is made by counting the number of hits. The calculated shower position will be between the two showers, so the fraction of the number of hits contained in the area of the shower position will be smaller than for events with one particle. Finally events are selected if the shower position is within 10 mm in the x and y direction from the detector center. These selections are done after calibration for sensor sensitivity.

To determine the shower position, the sensors first need to be aligned. This is done using muon tracks from cosmic ray measurements at Utrecht. Misalignment is described by movements in the x and y directions and a rotation θ around the z axis. After alignment, the approximate shower position in early layers (layer 3 and 4) is determined and compared to the position in layer 0. To determine the shower position, first the center of gravity of the hits in layer 3 and 4 is calculated. Then the search range is reduced and the center is calculated again, in order to counter noise. Afterwards the information of layers 3 and 4 is combined and the final shower position is calculated for layer 0 by searching for clusters within 1 mm of the position from layers 3 and 4. After calibration, the procedure of calculating the center of gravity of hits is repeated, since the sensor sensitivities are not identical. The inclination of the beam is determined by using tracks from the beam.

The lateral hit densities are calculated as a function of the distance r to the shower axis and by counting the number of hits. For each layer, the area is divided in rings around the shower axis and the hit density $\rho_{l,q}$ in a sensor (l, q) is calculated as:

$$\rho_{l,q}(r) = \frac{\Delta N^{l,q}_{hits}(r) - \Sigma p_i}{\Delta N^{l,q}_{pixels}(r) \cdot (30\mu\mathrm{m})^2} \tag{12}$$

Here $\Delta N^{l,q}_{hits}(r)$ is the number of hits in a ring for a given sensor, $\Delta N^{l,q}_{pixels}(r)$ is the number of live pixels within the ring and Σp_i is the total noise contribution, obtained by summing the noise probability p_i over all live pixels. Areas where sensors overlap or which are dead areas, are accounted for by using the number of hits and the area of the live areas. The step size of the rings is 0.1 mm for $r \leq 2$ mm and 0.5 mm for $r > 2$ mm, to get more details of the shower development, escpecially in the shower core.

Calibration is based on measurements of hit density distributions in longitudinal and lateral directions, using all selected events at a certain energy. First the response is equalised in each layer, then inter-layer calibration is done by fitting longitudinal profiles. If the shower center happens to be in a dead area, an extrapolation method is used for the hit densities after calibration. This method calculates the number of hits per ring depending on the number of live pixels ΔN_{pixel}. If $\Delta N_{pixel} > 0$, then the hit density of the dead area is assumed to be the same as for live areas with the same distance to the shower axis. The number of hits will be calculated by multiplying the density and the area of the ring. If $\Delta N_{pixel} = 0$, then the hit density is estimated from the densities in the previous and next layer. For a more detailed description of the earlier analysis, refer to [10].

4.2 Calculating new uncertainties

Due to a disk failure, the original data have been lost. The data used for this thesis were intermediate data, which contained the hit densities as given in equation 12 without uncertainties. The method used to estimate new uncertainties assumes pure Poisson fluctuations of the number of hits with a constant mean value event by event. We start by recalculating the mean number of hits N_{hits} in a ring at distance r_i from the shower center by multiplying the density ρ_i with the area of the ring:

$$N^i_{hits} = \rho_i \cdot 2\pi(r_i^2 - r_{i-1}^2) \tag{13}$$

For the first ring there is no r_{i-1}, leading to an area of $2\pi r_0^2$. The next rings have r_i increased by the step size and a total area of a circle with radius r_i minus the area of a circle with radius r_{i-1}. If all events have the same mean number of hits, the spread of the number of hits is $\sqrt{N_{hits}}$ and the uncertainty of the mean would be $\sqrt{N_{hits}/N_{events}}$. The relative uncertainty is thus $1/\sqrt{N_{hits} \cdot N_{events}}$. However, this does not cover everything. In general, also the mean will vary event by event causing a larger uncertainty. This is impossible to estimate from the available data, but it is clear that the error above is too small. What is important to correctly perform a fit, i.e. correctly weigh the different parts of the data, is that the relative variation of the uncertainty is correct. We can assume that this relative variation is correctly given by the Poisson term, which varies only from the factor $1/\sqrt{N_{hits}}$, since N_{events} is the same for all values of radius r. So we use as a different assumption just this term as relative uncertainty for calculating the uncertainty of the hit densities. Using the formula from appendix A for calculating uncertainties of quantities produced by multiplication, we get an uncertainty for the density:

$$\delta\rho_i = |\rho_i| \cdot \frac{\delta N^i_{hits}}{N^i_{hits}} = \frac{|\rho_i|}{\sqrt{N^i_{hits}}} \tag{14}$$

The new calculated uncertainties are probably too large, since further calculations, using these uncertainties, result in very high uncertainties. See the lower part of figure 9 for an example. The bin-by-bin fluctuations are much smaller than the errorbars. Because of these high uncertainties, it is difficult to interpret the χ^2 obtained from the fits, which will be discussed in section 4.4.

4.3 Fitting Lateral Profiles

For $r > 20$ mm, noise levels begin to intervene with the data, so the profiles are shown only for $r \leq 20$ mm and layer 0 was not used for fits. In figure 3 we already saw that the data is not linear on a logarithmic scale. As a check, first some fits were performed using 'simple' functions:

- A single exponent:

$$h_1(r) = e^{(p_0 + p_1 r)} \tag{15}$$

- A Gaussian:

$$h_2(r) = p_0\ e^{(-\frac{1}{2}(\frac{r-p_1}{p_2})^2)} \tag{16}$$

- A polynomial of degree 9:

$$h_3(r) = p_0 + p_1 r + p_2 r^2 + p_3 r^3 + p_4 r^4 + p_5 r^5 + p_6 r^6 + p_7 r^7 + p_8 r^8 + p_9 r^9 \tag{17}$$

The results of these fits are shown in figure 8. The lower part shows the relative deviation of the fit for each data point, calculated with $d^i_l(r) = \frac{\rho^i_l - \rho^i_{fit}}{\rho^i_{fit}}$, where ρ^i_{fit} and ρ^i_l are the density predicted by the fit and the measured density respectively. For a good result, the deviations should be as close to 0 as possible. As expected from the theory, the density can not be described by these functions. The Gaussian and single exponential show almost the same behaviour and do not show the curvature found in the measurements. For the polynomial we see a better description, but with an oscillation in the relative deviation. This oscillation is not seen in the behaviour of the data and thus can be seen as unphysical, so it is also not a good fit.

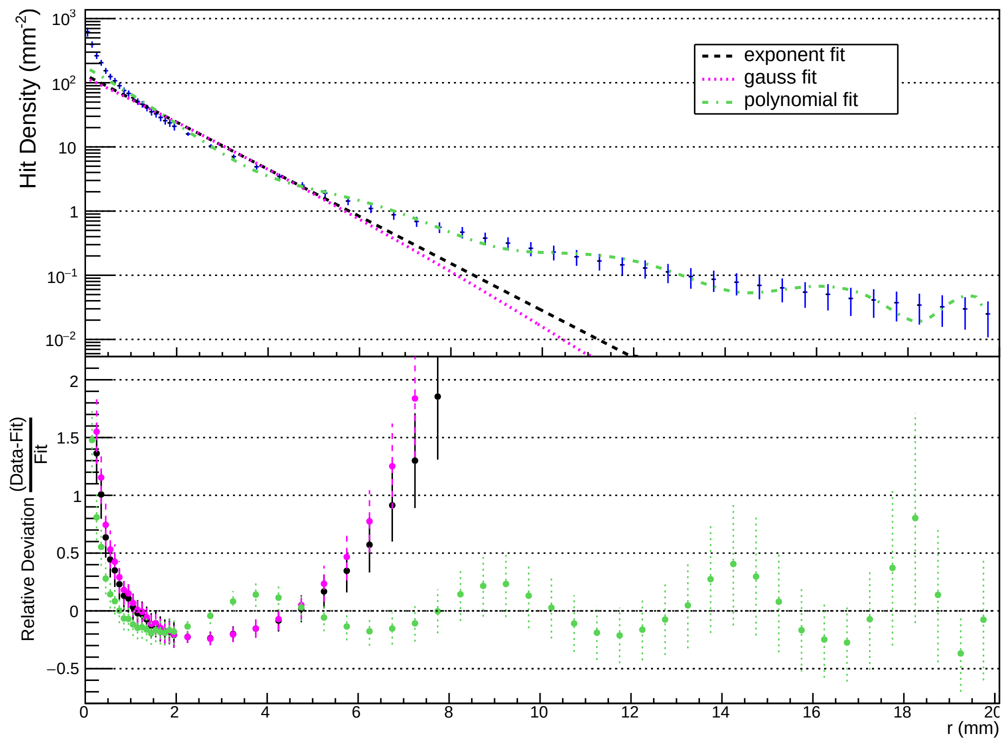

Figure 8: Comparison of the lateral profiles with 3 fits in layer 8 for 50 GeV. The lower panel shows the relative deviation of the fits. Color schemes are the same for both panels.

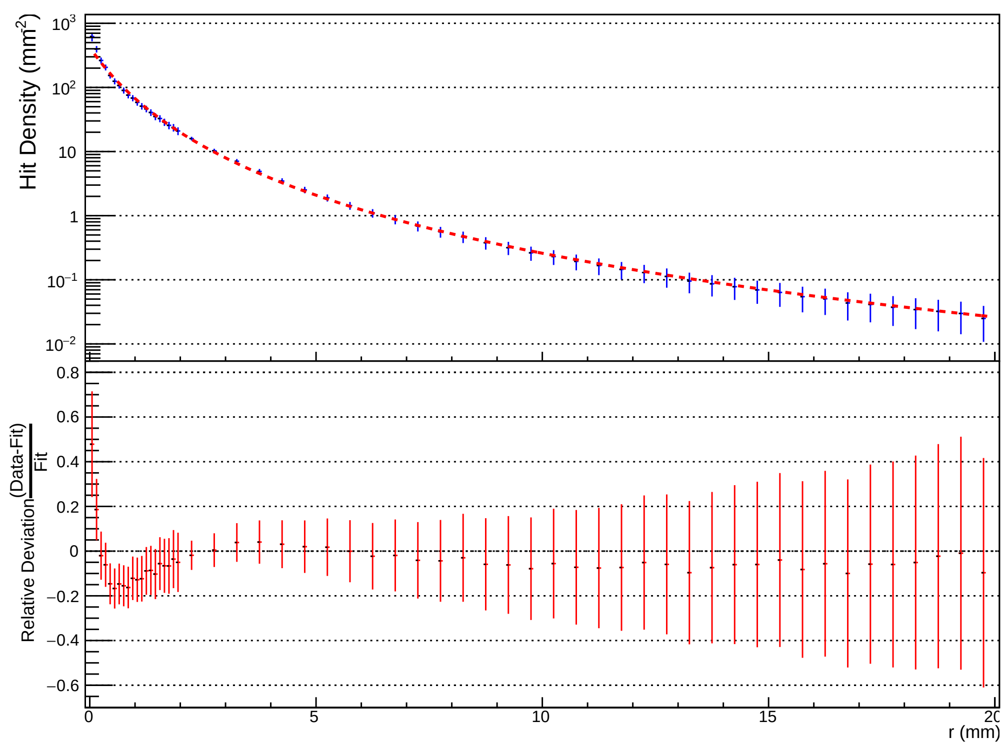

Figure 9: Top: fit result of $g_0(r)$ (equation 11) in layer 8 for 50 GeV. Bottom: relative deviation of $g_0(r)$ in layer 8 for 50 GeV.

The equations discussed in section 2.3.1 have been suggested to fit the profiles and in [10] it was concluded that the power law function, $g_0(r)$ (equation 11), describes the data best, so it was used for further analysis. From the fit with $g_0(r)$, relative deviations were calculated, seen in figure 9. In the figure you can see the fit starts too low for the first rings, following an overestimation in the next rings. A small dip occurs between $r = 3$ mm and $r = 6$ mm, after which the fit is overestimating the density again. It is clear the function used is not yet perfect to describe the measured densities, so adjustments could be tried.

General adjustments can be done by defining a function $\epsilon(r)$, assumed to be small, and implementing it in $g_0(r)$ in several ways:

- Adjusting the inner part of $g_0(r)$: $g_0'(r) = p_0(1 + \epsilon(r) + \frac{r}{p_1 p_2})^{-p_1}$
- Adding/subtracting a corrective function: $g_0'(r) = g_0(r) + \epsilon(r)$
- Multiplying a corrective function: $g_0'(r) = g_0(r) \cdot (1 + \epsilon(r))$

From the behaviour of the relative deviations several ideas were formed. These ideas were used to make the following adjustments:

- A power law function with a polynomial inside:

$$g_1(r) = p_0(1 + p_3 r^2 + p_4 r^3 + \frac{r}{p_1 p_2})^{-p_1} \tag{18}$$

- A power law function with a correction:

$$g_2(r) = g_0(r) + g_{corr}(r) = p_0(1 + \frac{r}{p_1 p_2})^{-p_1} + p_3(1 + \frac{r}{p_4 p_5})^{-p_4} \tag{19}$$

  This function is applied in two ways. One way fits the first term without correction over a range of 0 mm $\leq r \leq$ 5 mm first. Then the parameters p_0, p_1 and p_2 are fixed and the function is fitted with correction over the whole range. The second way uses the resulting parameters from the original $g_0(r)$ fit, fixes them and then fits with correction over the whole range.

- A power law function multiplied by a polynomial:

$$g_3(r) = g_0(r) \cdot (1 + p_3 r + p_4 r^2 + p_5 r^3) \tag{20}$$

  This function is also applied in two ways. The first way fits the function over the whole range with all parameters free. The second way uses the resulting parameters from the $g_0(r)$ fit, fixes them and then fits over the whole range.

- A power law multiplied by a Lennard-Jones-like potential:

$$g_4(r) = g_0(r) \cdot (1 - \frac{p_3}{r^{12}} + \frac{p_4}{r^6}) \tag{21}$$

  For this function the parameters resulting from the $g_0(r)$ fit are used and fixed and then the function is fitted over the whole range.

4.4 Results

The results of the fits with adjusted functions can been seen in figure 10. The results for $g_1(r)$ (figure 10a) show the function has trouble with the $r < 1$ mm range, but it does better for $r > 1$ mm. Compared to $g_0(r)$ the deviations are closer to 0 for $g_1(r)$ for the most part, especially the tail. The results of the first way to apply $g_2(r)$ (figure 10b) seem to be a better description for the core, but the function fails to adjust for the tail. It also has an oscillating effect in the deviation. It seems this method is not good enough to continue with. The results of the second way to apply $g_2(r)$ (figure 10c) show similar behaviour as $g_1(r)$. The function has some trouble with the first ring, but seems to have its deviations more centered around 0.

Looking at the results of $g_3(r)$ using the first method (figure 10d), we see it performs well for $r < 3$ mm, but has trouble with the tail. The deviations show similar behaviour as $g_0(r)$, but grow larger for $r > 14$ mm. However, when comparing it to the second method (figure 10e), it is not immediatly clear which performs better, since the second method seems to have more trouble with the core. The deviations are slightly larger for $r < 4$ mm, but are much smaller for $r > 4$ mm. Also, the deviations seem to be centered more around 0 than for $g_0(r)$. Finally, the results from $g_4(r)$ (figure 10f) show high deviations in the first two rings, but the function performs slightly better for the other rings compared to $g_0(r)$. By just looking at the deviations, it is not immediatly clear which fit performs better.

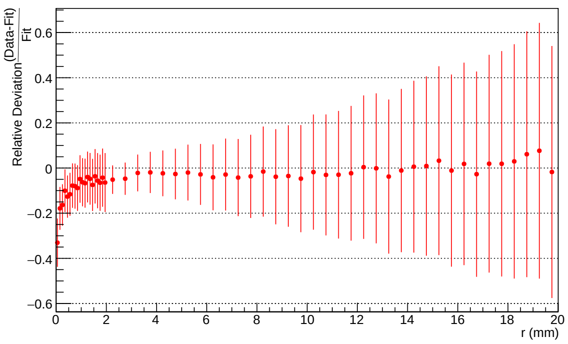

(a)

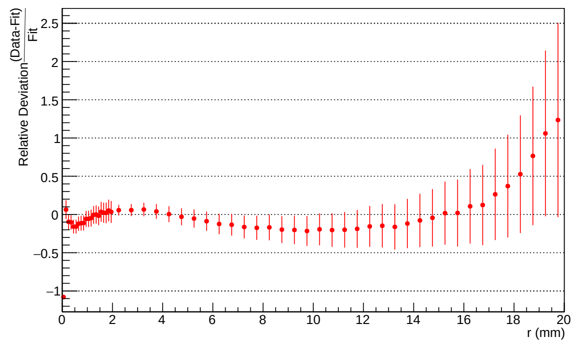

(b)

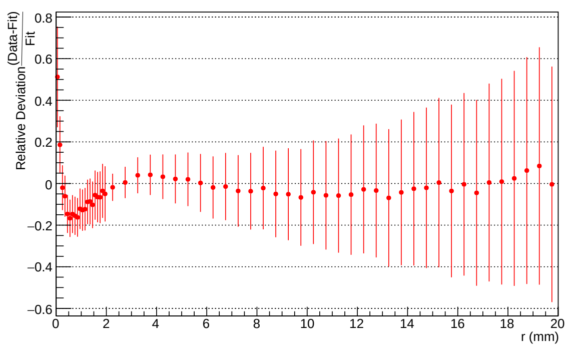

(c)

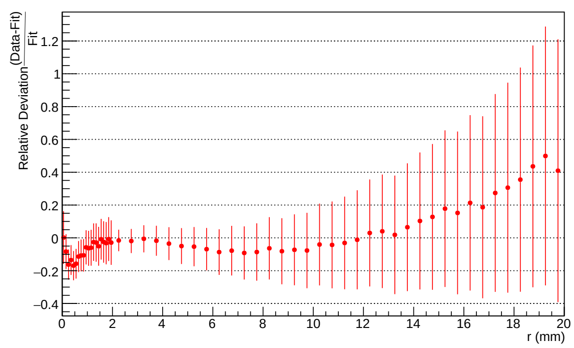

(d)

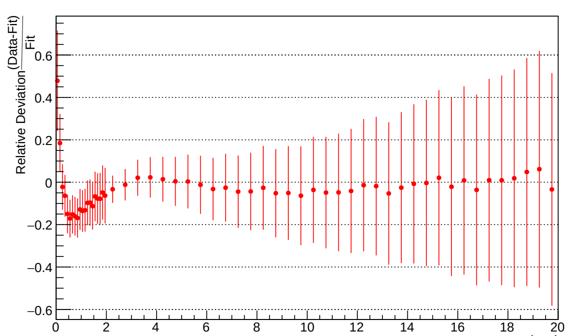

(e)

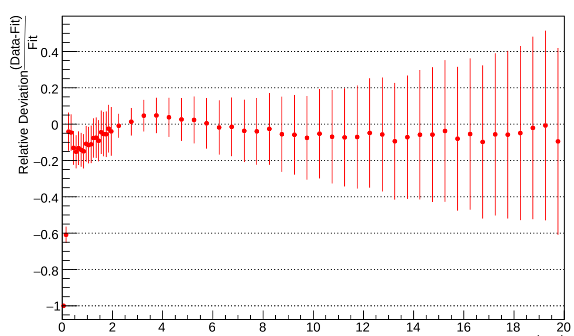

(f)

Figure 10: Results for all fits with adjusted functions in layer 8 for 50 GeV. a): $g_1(r)$ (equation 18). b): $g_2(r)$ (equation 19) first method. c): $g_2(r)$ second method. d): $g_3(r)$ (equation 20) first method. e): $g_3(r)$ second method. f): $g_4(r)$ (equation 21).

A way to compare the fit results is looking at the χ^2 of each fit. In general, a lower χ^2 would mean a better fit. The results can been seen in figure 11. For $g_2(r)$ only the results of the second method were used, since the first method did not seem to perform well. For $g_3(r)$ both methods were studied, indicated by $g_{3,1}(r)$ and $g_{3,2}(r)$ for the first and second method respectively. The χ^2 seems to vary a lot per layer for all functions. It seems all functions have more trouble fitting layers $3-7$ than the other layers. All adjustments seem to perform better than $g_0(r)$, with only a few exceptions for the later layers, e.g. layer 17, where $g_2(r)$ pops up. The lowest χ^2 values can be found for $g_1(r)$, with the exception of layer 2. This would imply that equation 18 would be the best fit. It also seems to have the least fluctuations in χ^2 for layers $7-23$. See appendix B for the resulting fit parameters of all performed fits.

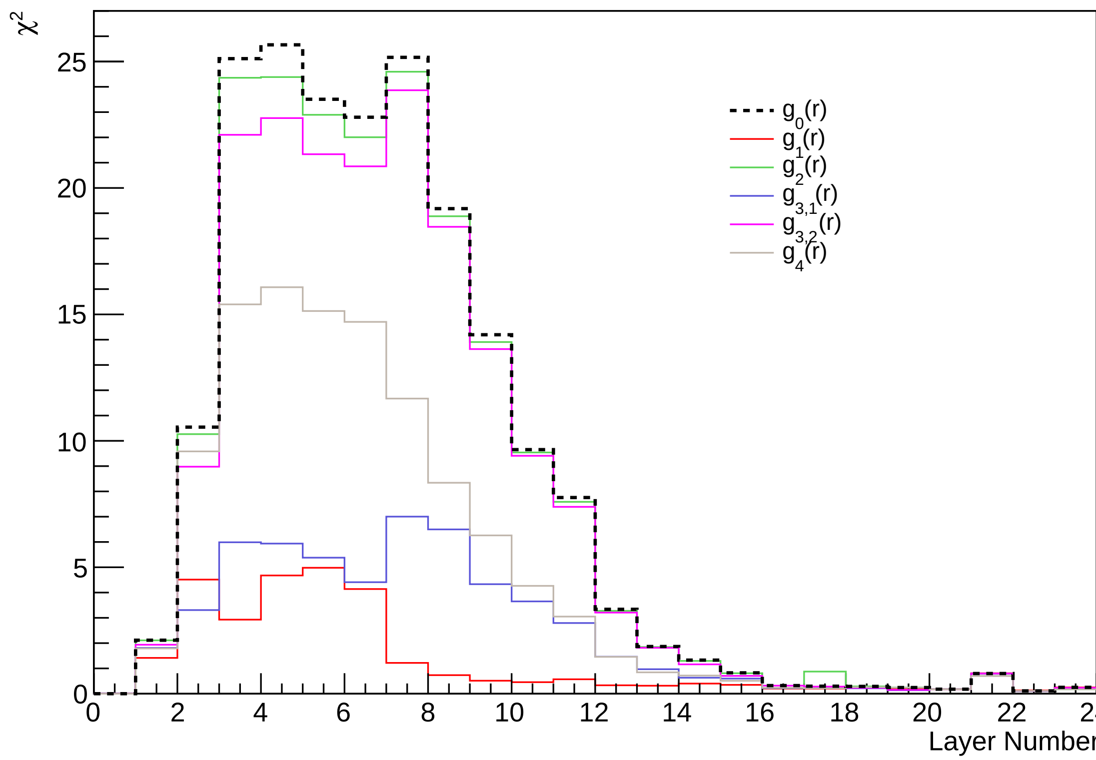

Figure 11: χ^2 of all fits in each layer at 50 GeV.

As discussed in section 4.2, the used uncertainties are currently being overestimated. On the other hand, adding N_{events} in the calculations for new uncertaintes would lead to too small uncertainties. In figure 12a you can see the relative deviation of the fit from $g_1(r)$ using smaller uncertainties for the data. It is clear the uncertainties are very small compared to figure 10a. However, it seems the relative deviation has roughly the same shape as before. The χ^2 of the fits with these smaller uncertaintes, seen in figure 12b, have much higher values, but they also show the same relative behaviour between the functions. This could indicate that the used functions are good options to describe the data.

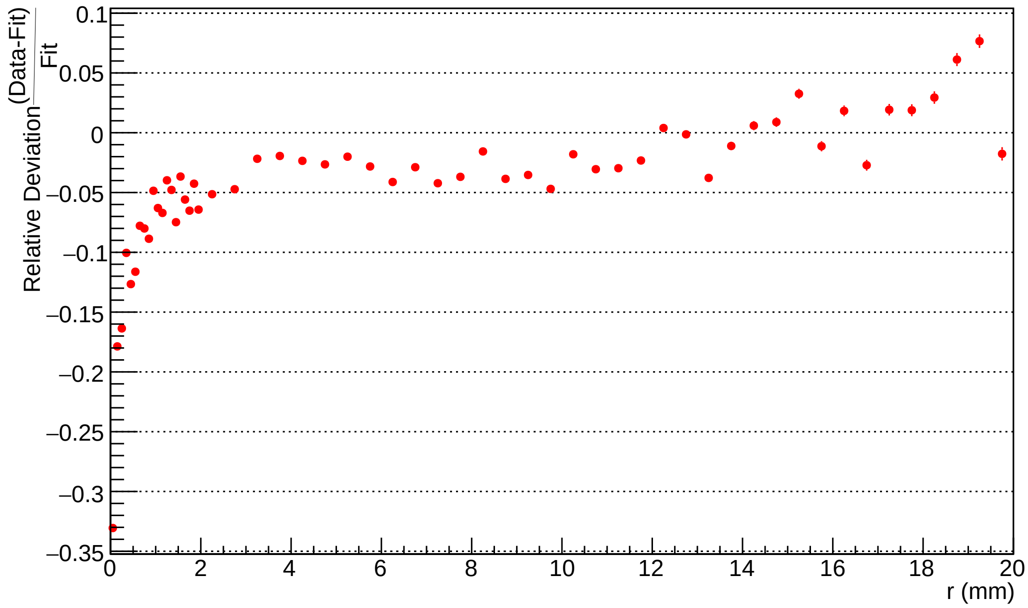

(a) Relative deviation of $g_1(r)$ in layer 8 for 50 GeV.

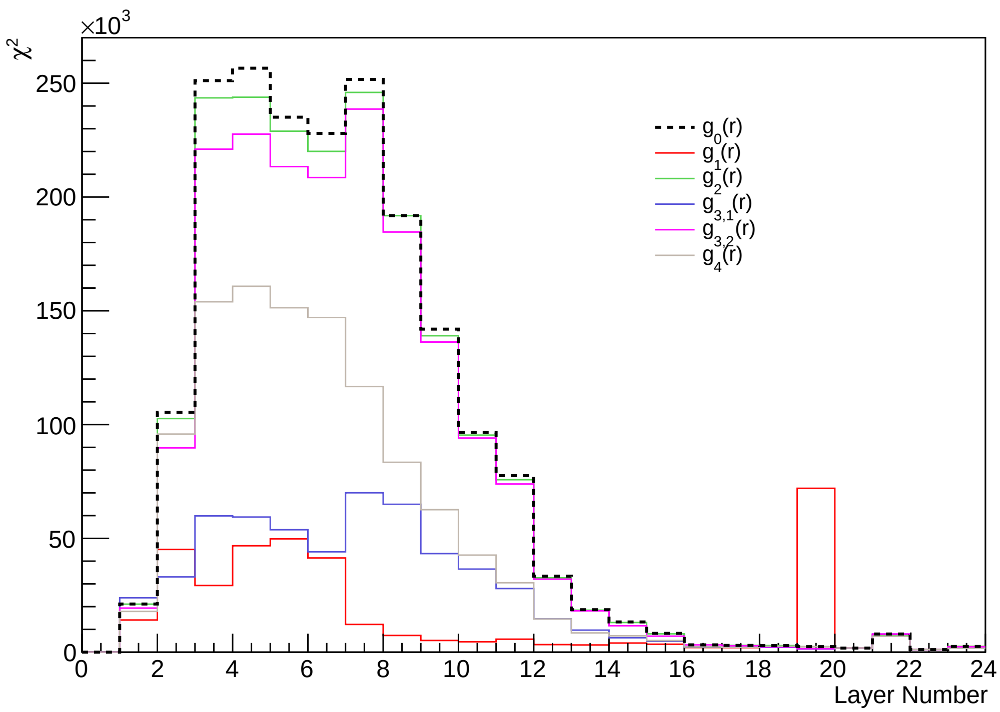

(b) χ^2 of all fits in each layer at 50 GeV.

Figure 12: Fit results using uncertainties calculated by including the N_{events} term.

5 Conclusion

The 50 GeV SPS data, taken with the FoCal prototype detector has been analysed by studying lateral hit density profiles, which were created in earlier analysis. New uncertainties for the lateral hit density profiles were calculated and new fit possibilities were tested. The calculated uncertainties are higher than the ones obtained by earlier analysis, indicating an overestimation of the new uncertainties. As expected, results of the single exponent functions and the polynomial (equations 15, 16 and 17) are confirmed to be bad fits for the data. The relative deviations of the fits with the powerlaw function $g_0(r)$ (equation 11), show that it does not describe the data well enough.

The adjustments applied to $g_0(r)$ were used to fit the profiles and the results were compared by looking at the relative deviations and the χ^2 of each fit. All adjusted functions generally show smaller deviations than the original, although some have larger deviations for the core or tail part. The $g_1(r)$ (equation 18), $g_{3,1}(r)$ (equation 20) and $g_4(r)$ (equation 21) functions seem better to describe the shower core, with the exception that $g_4(r)$ is not good for the first two rings. Only $g_{3,1}(r)$ does not seem to describe the shower tail well.

The χ^2 for each fit in figure 11 suggests that the adjustments give better results than the original function. It also shows that each function has more trouble fitting the middle layers (layers $3-7$). Overall it seems $g_1(r)$ has the best results, since it has the lowest χ^2 of all functions. However, due to the new calculated uncertainties, it is difficult to make definitive conclusions. Comparing the results to the results of data with N_{events} included in uncertainty calculation, the same behaviour of the functions is found. This could mean the functions are good to describe the data.

For future research, other adjustments for the power law function $g_0(r)$ could be tried. Further analysis could also include the longitudinal behaviour of the shower to obtain a fully three-dimensional description of showers. Another way to continue research is by looking at new ways of calculating the uncertainties for hit densities, or redoing the earlier analysis. With better uncertainties it might be possible to revisit the adjusted functions tried in this thesis, leading to clearer results. Additionally, other energies can be studied to see if the adjusted functions perform well for those energies.

A General Uncertainty Calculation

As stated in section 1, new uncertainties were calculated during data analysis. This section briefly explains several ways to do that. In general, when quantities with uncertainties are used to calculate new values, the uncertainties need to be correctly combined. The method to do so depends on the type of function used for calculation. These methods are:[11]

- **Addition of quantities:** when using measured quantities A and B with uncertainties δA and δB, the final result $C = A + B$ will have uncertainty $\delta C = \sqrt{(\delta A)^2 + (\delta B)^2}$. An approximation can be made as upper bound for δC with $\delta C \approx \delta A + \delta B$.
- **Multiplication of quantities:** using the same symbols as for addition, the final result $D = \frac{A \cdot B}{C}$ will have uncertainty $\delta D = |D|\sqrt{(\frac{\delta A}{A})^2 + (\frac{\delta B}{B})^2 + (\frac{\delta C}{C})^2}$. In this case you can approximate it with $\frac{\delta D}{|D|} \approx \frac{\delta A}{|A|} + \frac{\delta B}{|B|} + \frac{\delta C}{|C|}$ as upper bound.
- **Multiplication with constants:** when multiplying a quantity A with a constant c to get $B = c \cdot A$, the uncertainty becomes $\delta B = |c| \cdot \delta A$.
- **Polynomial functions:** for quantities calculated by polynomial functions ($B = A^n$), the uncertainty can be calculated using $\delta B = |n| \cdot |B| \cdot \frac{\delta A}{|A|}$. This can be used for positive and negative values of n.
- **Other functions:** if the above methods do not apply to the function used for calculation, then the general way to calculate the uncertainty of a function $D(A, B, C)$ is $\delta D = \sqrt{(\frac{\partial D}{\partial A} \cdot \delta A)^2 + (\frac{\partial D}{\partial B} \cdot \delta B)^2 + (\frac{\partial D}{\partial C} \cdot \delta C)^2}$.

B Fit Parameters

Table 1: Fit parameters of $g_0(r)$ and $g_1(r)$ for each layer at 50 GeV. (*fit was not fully minimised by the software.)

	$g_0(r)$			$g_1(r)$				
Layer	p_0	p_1	p_2	p_0	p_1	p_2	p_3	p_4
1	7.86184×10^3	2.05462	4.37801×10^{-3}	3.89255×10^5	1.80362	3.68671×10^{-4}	2.34600×10^2	-9.89088 *
2	8.94147×10^2	2.52089	5.49550×10^{-2}	2.49562×10^3	1.56234	1.79872×10^{-2}	1.78604×10^1	6.01085×10^{-3}
3	7.42827×10^2	3.08464	1.40744×10^{-1}	4.54830×10^3	1.18706	1.50041×10^{-2}	2.46837×10^1	1.77374×10^1
4	7.70516×10^2	3.36975	2.05111×10^{-1}	1.67584×10^3	1.33011	6.94219×10^{-2}	4.47485	1.47132
5	7.74169×10^2	3.45735	2.56883×10^{-1}	1.44558×10^3	1.27898	9.93935×10^{-2}	2.97672	1.13902
6	6.95532×10^2	3.51039	3.00336×10^{-1}	1.23183×10^3	1.29376	1.24386×10^{-1}	2.04981	6.85418×10^{-1}
7	5.30300×10^2	3.67004	3.74830×10^{-1}	1.20292×10^3	1.21678	1.04799×10^{-1}	9.66607×10^{-1}	1.01652
8	4.20566×10^2	3.67124	4.19863×10^{-1}	9.28760×10^2	1.17006	1.14846×10^{-1}	6.20551×10^{-1}	9.87603×10^{-1}
9	3.10615×10^2	3.64568	4.66473×10^{-1}	6.36588×10^2	1.16043	1.39208×10^{-1}	5.67841×10^{-1}	6.93496×10^{-1}
10	2.09216×10^2	3.69193	5.53414×10^{-1}	4.07307×10^2	1.12444	1.67075×10^{-1}	2.49583×10^{-1}	5.45565×10^{-1}
11	1.32808×10^2	3.61674	6.39416×10^{-1}	2.61371×10^2	1.10268	1.88127×10^{-1}	2.03754×10^{-1}	3.81167×10^{-1}
12	1.04178×10^2	3.59275	6.70481×10^{-1}	1.64975×10^2	1.08620	2.65249×10^{-1}	2.96667×10^{-1}	2.84172×10^{-1}
13	6.94765×10^1	3.51525	7.38115×10^{-1}	1.02008×10^2	1.04944	3.20140×10^{-1}	2.71645×10^{-1}	2.31637×10^{-1}
14	4.39621×10^1	3.47235	8.28539×10^{-1}	5.98011×10^1	1.07696	4.25073×10^{-1}	2.89907×10^{-1}	1.15251×10^{-1}
15	2.89385×10^1	3.35853	8.98794×10^{-1}	3.73838×10^1	1.04311	4.99903×10^{-1}	2.80278×10^{-1}	9.31062×10^{-2}
16	1.98626×10^1	3.16305	9.20479×10^{-1}	2.31204×10^1	9.88621×10^{-1}	6.20083×10^{-1}	3.32439×10^{-1}	8.65223×10^{-2}
17	1.25327×10^1	3.16698	1.04908	1.49308×10^1	9.52700×10^{-1}	6.50685×10^{-1}	2.40012×10^{-1}	8.09044×10^{-2}
18	7.39908	3.16176	1.20747	7.86385	1.34735	1.06750	1.05850×10^{-1}	2.67380×10^{-3} *
19	5.17453	2.93816	1.20085	5.50899	1.24568	1.05588	1.28292×10^{-1}	3.36272×10^{-3} *
20	3.02428	2.81572	1.33992	3.10160	9.87785×10^{-1}	1.26616	1.90142×10^{-1}	1.29546×10^{-2}
21	1.75148	2.69671	1.49829	1.56395	7.46605×10^{-1}	2.14396	2.21831×10^{-1}	5.02000×10^{-2}
22	1.03176×10^{-1}	2.23602	2.55452	7.48770×10^{-2}	6.44951×10^{-1}	2.19012×10^2	1.41421×10^{-1}	5.91391×10^{-3}
23	5.92500×10^{-2}	2.55852	3.48203	5.28461×10^{-2}	6.84340×10^{-1}	9.01385	8.89895×10^{-2}	3.13197×10^{-3}

Table 2: Fit parameters of $g_2(r)$ for each layer at 50 GeV. (*fit was not fully minimised by the software.)

	$g_2(r)$		
Layer	p_3	p_4	p_5
1	-3.87200×10^3	1.19691	4.06649×10^{-6}
2	-3.70836×10^2	8.57201×10^{-1}	4.60370×10^{-6}
3	-2.64135×10^2	7.89640×10^{-1}	5.82824×10^{-6}
4	-4.41920×10^1	4.65953×10^{-1}	3.89091×10^{-8}
5	-9.49302	6.93435×10^{-1}	1.96958×10^{-4}
6	-1.79624×10^1	4.14684×10^{-1}	5.37091×10^{-8}
7	-4.00883	3.33032×10^{-1}	3.40247×10^{-8}
8	-7.10798	2.90857×10^{-1}	1.14406×10^{-10}
9	-8.30313×10^{-2}	1.44071×10^{-1}	8.09545×10^{-9} *
10	-4.84204	2.05504×10^{-1}	2.15325×10^{-15} *
11	-7.72236	1.71644×10^{-1}	3.72981×10^{-19} *
12	-1.37902×10^{-3}	2.53163×10^{-4}	3.31694×10^{-5} *
13	-8.80224×10^{-4}	1.79614×10^{-4}	3.02600×10^{-7} *
14	-1.40292	3.21450×10^{-1}	6.92716×10^{-9} *
15	-1.88515	3.67676×10^{-1}	1.75955×10^{-8} *
16	7.59702	3.00069×10^3	1.00437×10^{-1}
17	9.96394×10^{-1}	-1.97969×10^1	9.98109×10^{-1} *
18	-1.23530×10^1	9.47291×10^{-1}	4.85141×10^{-5} *
19	-1.42291×10^{-2}	5.50574×10^{-1}	9.82595×10^{-3} *
20	-1.53515	1.03352	1.98239×10^{-4}
21	-2.23727×10^3	1.47469	1.09196×10^{-4}
22	-1.72467×10^2	6.61179	2.62691×10^{-3}
23	-9.74911	3.14121	3.81895×10^{-3}

Table 3: Fit parameters of $g_3(r)$ (first method) for each layer at 50 GeV. (*fit was not fully minimised by the software.)

Layer	$g_{3,1}(r)$ p_0	p_1	p_2	p_3	p_4	p_5
1	-1.30497×10^3	2.95797	5.03589×10^{-4}	-9.41874×10^4	7.48542×10^3	-4.25330×10^2 *
2	2.05253×10^3	1.82145	2.34073×10^{-2}	-2.14409×10^{-1}	1.69151×10^{-2}	-4.27266×10^{-4}
3	1.64499×10^3	1.92403	6.17118×10^{-2}	-2.07950×10^{-1}	1.53205×10^{-2}	-3.68746×10^{-4}
4	1.28762×10^3	2.06946	1.15811×10^{-1}	-1.92873×10^{-1}	1.34837×10^{-2}	-3.14127×10^{-4}
5	1.15809×10^3	2.09840	1.60850×10^{-1}	-1.85217×10^{-1}	1.26195×10^{-2}	-2.87637×10^{-4}
6	1.02589×10^3	2.06287	1.89408×10^{-1}	-1.79549×10^{-1}	1.19508×10^{-2}	-2.68670×10^{-4}
7	8.18632×10^2	1.96981	2.23577×10^{-1}	-1.78666×10^{-1}	1.16956×10^{-2}	-2.59002×10^{-4}
8	6.12136×10^2	1.96262	2.66096×10^{-1}	-1.73871×10^{-1}	1.12452×10^{-2}	-2.47647×10^{-4}
9	4.45043×10^2	1.90406	2.97982×10^{-1}	-1.68661×10^{-1}	1.06809×10^{-2}	-2.32023×10^{-4}
10	2.82471×10^2	1.87863	3.77796×10^{-1}	-1.62750×10^{-1}	1.00651×10^{-2}	-2.15063×10^{-4}
11	1.84913×10^2	1.71502	4.11450×10^{-1}	-1.56835×10^{-1}	9.40272×10^{-3}	-1.96770×10^{-4}
12	1.27567×10^2	1.91018	5.20816×10^{-1}	-1.45737×10^{-1}	8.53369×10^{-3}	-1.77729×10^{-4}
13	8.13599×10^1	1.91676	6.11347×10^{-1}	-1.38375×10^{-1}	7.92836×10^{-3}	-1.63498×10^{-4}
14	5.13974×10^1	1.85813	6.88436×10^{-1}	-1.31053×10^{-1}	7.28112×10^{-3}	-1.48804×10^{-4}
15	3.08860×10^1	2.89443	8.18128×10^{-1}	-4.76307×10^{-3}	-1.50170×10^{-3}	4.23984×10^{-5}
16	2.15848×10^1	1.89852	8.53682×10^{-1}	-1.12067×10^{-1}	5.79720×10^{-3}	-1.12442×10^{-4}
17	1.34796×10^1	1.82836	1.00402	-1.14516×10^{-1}	6.15189×10^{-3}	-1.25634×10^{-4}
18	7.70750	3.29105	1.05693	6.43733×10^{-2}	-1.99663×10^{-3}	-7.23805×10^{-7}
19	5.26206	3.27949	1.18805	3.17925×10^{-3}	3.83262×10^{-3}	-1.63727×10^{-4}
20	3.05494	2.78137	1.31732	9.35954×10^{-4}	9.56175×10^{-5}	-9.85337×10^{-5}
21	1.76192	2.60128	1.43416	1.57802×10^{-2}	-1.96655×10^{-3}	6.21067×10^{-5} *
22	9.74857×10^{-2}	4.65539	4.18056	-8.40498×10^{-2}	7.83382×10^{-3}	-1.88931×10^{-4} *
23	6.12768×10^{-2}	4.35166×10^1	7.65877	-1.35489×10^{-1}	1.17275×10^{-2}	-3.09862×10^{-4} *

Table 4: Fit parameters of $g_3(r)$ (second method) and $g_4(r)$ for each layer at 50 GeV.

Layer	$g_{3,2}(r)$ p_3	p_4	p_5	$g_4(r)$ p_3	p_4
1	2.36163×10^{-2}	-8.12636×10^{-3}	4.21032×10^{-4}	-4.26979×10^{-14}	-2.73194×10^{-6}
2	7.58742×10^{-2}	-1.63384×10^{-2}	6.75967×10^{-4}	-1.98077×10^{-15}	-1.23459×10^{-7}
3	5.93952×10^{-2}	-1.25630×10^{-2}	4.98672×10^{-4}	2.32052×10^{-14}	1.49554×10^{-6}
4	3.56345×10^{-2}	-6.67376×10^{-3}	2.25195×10^{-4}	5.30419×10^{-14}	3.40099×10^{-6}
5	2.71826×10^{-2}	-5.57489×10^{-3}	2.12808×10^{-4}	4.99696×10^{-14}	3.20304×10^{-6}
6	2.02429×10^{-2}	-3.68659×10^{-3}	1.22641×10^{-4}	5.21802×10^{-14}	3.34424×10^{-6}
7	1.42788×10^{-2}	-2.45635×10^{-3}	7.54851×10^{-5}	6.11513×10^{-14}	3.92379×10^{-6}
8	1.04996×10^{-2}	-1.78571×10^{-3}	5.51145×10^{-5}	5.85683×10^{-14}	3.75872×10^{-6}
9	7.45567×10^{-3}	-1.02246×10^{-3}	2.08047×10^{-5}	6.08394×10^{-14}	3.90338×10^{-6}
10	5.23227×10^{-3}	-7.35283×10^{-4}	1.68828×10^{-5}	5.74191×10^{-14}	3.68475×10^{-6}
11	31.0276×10^{-3}	3.59824×10^{-4}	-3.51516×10^{-5}	6.80853×10^{-14}	4.36943×10^{-6}
12	3.31519×10^{-4}	2.89142×10^{-4}	-2.45448×10^{-5}	4.72546×10^{-14}	3.03199×10^{-6}
13	5.13397×10^{-5}	2.23896×10^{-4}	-1.72881×10^{-5}	4.02495×10^{-14}	2.58299×10^{-6}
14	-3.68294×10^{-3}	1.12053×10^{-3}	-5.88310×10^{-5}	3.93673×10^{-14}	2.52614×10^{-6}
15	-4.27209×10^{-3}	1.16435×10^{-3}	-5.80841×10^{-5}	3.53355×10^{-14}	2.26704×10^{-6}
16	1.90743×10^{-4}	4.50547×10^{-5}	-4.43024×10^{-6}	1.92895×10^{-14}	1.23825×10^{-6}
17	-2.37664×10^{-3}	5.82383×10^{-4}	-2.75416×10^{-5}	3.03410×10^{-14}	1.94551×10^{-6}
18	-5.42454×10^{-3}	1.27161×10^{-3}	-5.86373×10^{-5}	7.64478×10^{-15}	4.93630×10^{-7}
19	-8.73570×10^{-3}	1.93399×10^{-3}	-8.62217×10^{-5}	4.53649×10^{-15}	2.91854×10^{-7}
20	-1.63294×10^{-3}	3.63392×10^{-4}	-1.62825×10^{-5}	-9.31074×10^{-15}	-5.96157×10^{-7}
21	2.02929×10^{-3}	-4.18724×10^{-4}	1.80136×10^{-5}	-7.75246×10^{-14}	-4.96038×10^{-6}
22	-3.44709×10^{-3}	6.18042×10^{-4}	-2.43344×10^{-5}	3.12266×10^{-14}	1.99510×10^{-6}
23	-2.14116×10^{-2}	3.85828×10^{-3}	-1.52115×10^{-4}	-5.65346×10^{-14}	-3.63316×10^{-6}

References

[1] The ALICE FoCal collaboration Letter of Intent, A Forward Calorimeter for the ALICE experiment (2010), https://indico.cern.ch/event/102718/contributions/14229/attachments/9309/13663/focal-loi-0-1.pdf.

[2] *The physics of particle detectors*, A course given by Prof. H.-C. Schultz-Coulon and Prof. J. Stachel (2011), http://www.kip.uni-heidelberg.de/~coulon/Lectures/Detectors/.

[3] J. Beringer et al. (Particle Data Group), Phys. Rev. D86, 010001 (2012), https://journals.aps.org/prd/pdf/10.1103/PhysRevD.86.010001.

[4] T. Mons, *Data analysis of focal at 244 gev using the hough transform and longitudinal profiles*, Bachelor's thesis at Utrecht University (2017), https://dspace.library.uu.nl/handle/1874/353040.

[5] H. Wang, *Prototype studies and simulations for a forward si-w calorimeter at the large hadron collider*, PhD thesis at Utrecht University (2018), https://dspace.library.uu.nl/handle/1874/358667.

[6] R. Wigmans, *Calorimetry - energy measurements in particle physics*, Oxford Science Publications (2000).

[7] G. Ferri, F. Groppi, F. Lemeilleur, S. Pensotti, P. G. Rancoita, A. Seidman, and L. Vismara, *The structure of lateral electromagnetic shower development in si/w and si/u calorimeters*, Nucl. Inst. Meth. A273 (1988), https://ac.els-cdn.com/0168900288908066/1-s2.0-0168900288908066-main.pdf?_tid=cd6b55fa-cabd-4d0c-87cb-aa5a61435d2b&acdnat=1528715947_bd17ca01cfd035c278c49cc6f4ef38b9.

[8] G. Grindhammer and S. Peters, *The parameterized simulation of electromagnetic showers in homogeneous and sampling calorimeters* (2000), https://arxiv.org/abs/hep-ex/0001020.

[9] R. Hagedorn, Riv. Nuovo Cim. 6 (1983), 1.

[10] C. Zhang, *Measurements with a high-granularity digital electromagnetic calorimeter*, PhD thesis at Utrecht University (2017), https://dspace.library.uu.nl/handle/1874/350040.

[11] *Error propagation*, Available from: http://lectureonline.cl.msu.edu/~mmp/labs/error/e2.htm (2018), accessed 17th May 2018.